Physics of Fluids

The response to external excitations in thermocapillary liquid layers

Cite as: Phys. Fluids **33**, 032104 (2021); https://doi.org/10.1063/5.0039833
Submitted: 07 December 2020 • Accepted: 25 January 2021 • Published Online: 02 March 2021

Kai-Xin Hu (胡开鑫), **Sheng Zheng** (郑晟) **and Qi-Sheng Chen** (陈启生)

The response to external excitations in thermocapillary liquid layers

Cite as: Phys. Fluids **33**, 032104 (2021); doi: 10.1063/5.0039833
Submitted: 7 December 2020 · Accepted: 25 January 2021 ·
Published Online: 2 March 2021

View Online Export Citation CrossMark

Kai-Xin Hu (胡开鑫),[1,a)] Sheng Zheng (郑晟),[1] and Qi-Sheng Chen (陈启生)[2,3]

AFFILIATIONS

[1] Key Laboratory of Impact and Safety Engineering (Ministry of Education), School of Mechanical Engineering and Mechanics, Ningbo University, Ningbo, Zhejiang 315211, China
[2] School of Engineering Science, University of Chinese Academy of Sciences, Beijing 100190, China
[3] Key Laboratory of Microgravity, Institute of Mechanics, Chinese Academy of Sciences, Beijing 100190, China

[a)] Author to whom correspondence should be addressed: hukaixin@nbu.edu.cn

ABSTRACT

The responses to external excitations in thermocapillary liquid layers are investigated by non-modal stability theory. The maximum amplification of input signals is measured by a response function depending on the perturbation velocity and temperature. There can be rather large amplifications in subcritical flows at both small and large Prandtl numbers (*Pr*). For small *Pr*, the response increases significantly with both the Reynolds number (*R*) and the Biot number (*Bi*) but decreases with *Pr*. The optimal response is achieved when the perturbation is almost a spanwise wave. The response properties for the linear flow and the return flow are similar. The amplification is caused by a combination of the lift-up mechanism, Orr mechanism, and external forcing. However, for large *Pr*, large amplifications could only be found in the return flow, while the variations of response with *Pr* and *Bi* are opposite to those at small *Pr*. The optimal response propagates in the streamwise direction. The amplification is caused by the thermocapillary effect.

I. INTRODUCTION

Thermocapillary convection, also called thermal Marangoni convection, is driven by the temperature-induced surface tension gradient. It plays an important role in many industrial applications, such as crystal growth,[1] inkjet printing,[2] droplet migration,[3] and nanofluid flows.[4] It is well known that a steady thermocapillary convection becomes unstable once the temperature difference exceeds a threshold. Abundant studies have been devoted to the instability of thermocapillary convection for its great practical importance. The related theoretical and experimental works have been reviewed by Davis[5] and Schatz and Neitzel,[6] respectively.

It has been found that there are two types of instabilities in thermocapillary convections, namely, stationary rolls and traveling waves.[7,8] The instability mechanisms at small and large Prandtl numbers are different. For the former, the perturbation energy mainly comes from the basic flow, and thus, the instability is purely hydrodynamic.[9] However, for the latter, the Marangoni force becomes the driving force for the perturbation, leading to the hydrothermal instability.[10] In some cases, the surface deformation is also related to instabilities.[11–13]

Recently, the investigation of thermocapillary instability has been extended to some new fields, such as thermocapillary flows in a circular film,[14] non-Newtonian fluid flows,[15–18] thermocapillary migration of droplets,[19] sideband thermocapillary instability,[20] and bifurcation routes to chaos.[21] It is also worth noting that the space experiment regarding the instability of thermocapillary convection in an open annular liquid pool has been carried out on the SJ-10 satellite of China,[22] which shows that the flow transition from the steady state to the oscillation state is accompanied by directional propagating hydrothermal waves with increasing temperature differences.

In the theoretical investigations of flow instabilities, the principal tool in determining the stability characteristics is the modal analysis, which assumes a small perturbation varying exponentially with time. The parameters of unstable hydrothermal waves in some thermocapillary convections obtained by modal analysis are comparable with both experiments[23] and numerical simulations.[24] The modal approach can also predict instability behaviors for other fluid systems, such as Rayleigh convection and Taylor–Couette flow.[25] However, in many cases, it fails to match most experimental results, especially in channel flows. For example, the modal analysis suggests that the plane Couette flow and the pipe Poiseuille flow are always stable at all Reynolds numbers,[26] which is unrealistic.

For this reason, some authors have turned to the non-modal stability theory,[27] which examines the short-term characteristics and the effect of background noise in flow transitions. The departure of the non-modal theory from the standard modal analysis is the fact that even if all eigenvalues of a linear operator are stable, the disturbance could be amplified substantially for a non-normal operator, whose eigenfunctions are non-orthogonal. The extent of non-normality of a linear operator can be seen from its pseudospectrum,[28] which demonstrates the response to external forcing with complex frequencies and also assesses the susceptibility of eigenvalues to disturbances.

As some experiments reported that transition scenarios often highly depend on the level of initial and external disturbances[29–32] and do not emanate from exponential instabilities predicted by modal analysis, Schmid and Henningson[26] have proposed the idea of bypass transition, which is emanated from non-modal growth mechanisms and bypasses the exponential instabilities. The amplifications of initial disturbances and external forcing can be measured in the non-modal approach by the transient growth and response functions, respectively.

There have been plenty of works on the non-modal stabilities. Trefethen *et al.*[28] have addressed the concept of non-modal stability in the study of shear flows. They found that both plane Couette and Poiseuille flow exhibit strong three-dimensional pseudo-resonance for a frequency of $\omega = 0$, while the magnitude is $O(R^2)$(R denotes the Reynolds number). Nouar *et al.*[33] have examined the receptivity problem of plane Bingham–Poiseuille flow with respect to weak perturbations. The pseudospectra they plotted demonstrate that the Bingham terms reduce the degree of non-normality. Liu and Liu[34] have investigated the non-modal stability in plane Couette flow of a power-law fluid and found that the shear thinning increases the amplitude of response, while the structures of the optimal input and output disturbances are similar to the Newtonian case. They have also generalized the non-modal approach to sliding Couette flow.[35] The results show that the response is sensitive to low-frequency external excitations, while the maximum response is achieved by non-axisymmetric and streamwise-independent disturbances when the frequency of external forcing is zero.

Although the modal analysis is the standard method to investigate thermocapillary instabilities in previous works, there is a need for the non-modal approach, which can be seen from three aspects. First, some critical Reynolds numbers R_c obtained by modal analysis are too high. Table I shows that $R_c \sim O(10^4)$ or $O(10^5)$ for some thermocapillary convections, which are much higher than the usual transition Reynolds numbers. For example, transitions to turbulence are observed in experiments for plane Poiseuille flow at $R \approx 1000$,[36] for plane Couette flow at $R \approx 360$,[37] for pipe Poiseuille flow at $R \approx 2000$,[38] for the flat-plate boundary layer at $R \approx 950$, and for Taylor-Couette flow at $R \approx 95$.[32] Therefore, it is reasonable to expect that subcritical instabilities may occur in thermocapillary convections.

TABLE I. Some critical Reynolds numbers R_c of thermocapillary convections obtained by modal analysis.

Flow	Pr	Bi	$R_c \times 10^{-4}$
Linear flow[7]	0.001	1	1.7
Return flow[7]	0.001	1	4.0
Liquid bridge[9]	0.5	0	1.03
Liquid pool[39]	0.03	0	3.88
	4	0	11.0

Second, some experimental studies demonstrate that there are many peaks in the frequency spectrum when the thermocapillary convection is just above the onset of instability.[40–42] So we should consider the evolution of a mixture of normal modes rather than just one in isolation. This idea is realized in the non-modal analysis. Third, the effectiveness of the non-modal approach in thermocapillary-driven flows has been supported by some experiments. For the contact line instability of thermocapillary spreading films, the experimentally measured values of transient amplification are comparable with the theoretical results obtained by non-modal analysis.[43–46] In the transient Rayleigh–Benard–Marangoni convection due to evaporation, good agreement was found between the non-normal approach and experimental observations.[47]

To the best of our knowledge, few works are available in the literature on the non-modal stability in thermocapillary convections. Our previous work[48] has examined the amplification of initial disturbances of thermocapillary liquid layers. It has been found that large transient growth occurs in subcritical flows at small Prandtl numbers, while the temperature field on the surface has a negative effect on the transient growth. As both the initial condition and background noise can control the transition Reynolds numbers, we would like to investigate the amplification of external forcing for thermocapillary liquid layers in this paper. The result shows the sensitivity of flow to external disturbances and the amplification mechanism, which will be useful to understand the instabilities and bypass transitions in thermocapillary convections.

This paper is organized as follows. Section II recalls the model of thermocapillary liquid layers. The dimensionless governing equations and boundary conditions are derived. The response function is defined. Section III is dedicated to the analysis of the maximum response function, pseudospectrum, and perturbation fields. Section IV is devoted to the amplification mechanism. Finally, the conclusions are itemized in Sec. V.

II. MATHEMATICAL FORMULATION

Figure 1 illustrates the physical model of thermocapillary liquid layers,[7] where an infinite fluid layer placed on a rigid plane is subjected to a constant temperature gradient $b = -\mathrm{d}T/\mathrm{d}x > 0$ on the free surface. *x*, *y*, and *z* are the streamwise, spanwise, and wall-normal direction, respectively. The surface tension σ' decreases with the temperature T: $\sigma' = \sigma'_0 - \gamma(T - T_0)$, where $\gamma = -\mathrm{d}\sigma'/\mathrm{d}T$. The linear flow has a uniform velocity gradient, while the return flow has zero mass flux in the vertical section.

A. Governing equations

The liquid layer is composed of the incompressible Newtonian fluid, whose viscosity μ, density ρ, thermal diffusivity χ, thermal conductivity $\hat{k}$, and unit thermal surface conductance $\hat{h}$ are supposed to be constant. $R = \rho\hat{U}_0 d/\mu$, $Ma = b\gamma d^2/(\mu\chi)$, $Pr = \mu/(\rho\chi)$, and $Bi = \hat{h}d/\hat{k}$ are the Reynolds number, Marangoni number, Prandtl number, and Biot number, respectively. Here, $\hat{U}_0 = b\gamma d/\mu$ is the velocity scale. It can be found that $Ma = R \cdot Pr$.

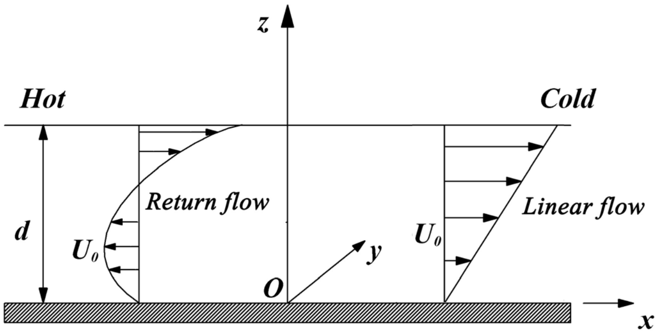

FIG. 1. Schematic of thermocapillary liquid layers: (a) the linear flow and (b) the return flow. Here, d is the depth of the layer, T_b is the temperature distribution in the vertical direction, and U_0 is the velocity field.

The magnitude of the surface deformation can be measured by the capillary number: $Ca = \mu \hat{U}_0/\hat{\sigma} = Ma/(Pr \cdot S)$, where $S = \rho d \hat{\sigma}/\mu^2$ is the non-dimensional surface-tension number. For liquid silicon,[7] $Pr = 0.023$, $S = 2.32 \times 10^6$, $Ma \sim 6.3$, and $Ca \sim 1.2 \times 10^{-4}$, while for silicone oil,[23] $Pr = 13.9$, $S \sim 25\,000$, and $Ca \sim 0.001$, which shows that Ca can be very small at both small and large Prandtl numbers. In order to study the amplification mechanism that is independent of the surface deformation, the free surface is assumed to be planar and non-deformable in the following.

The dimensionless forms of continuity equation, momentum equation, and energy equation can be expressed as

$$\nabla \cdot \mathbf{u} = 0, \tag{1}$$

$$R\left(\frac{\partial \mathbf{u}}{\partial t} + \mathbf{u} \cdot \nabla \mathbf{u}\right) = -\nabla p + \nabla \cdot \boldsymbol{\tau}, \tag{2}$$

$$\frac{\partial T}{\partial t} + \mathbf{u} \cdot \nabla T = \frac{1}{Ma} \nabla^2 T. \tag{3}$$

Here, $\mathbf{u}$, p, and T stand for the velocity, pressure, and temperature, respectively. $\boldsymbol{\tau}$ is the stress tensor. For Newtonian fluid,

$$\boldsymbol{\tau} = \mathbf{S}, \tag{4}$$

where $\mathbf{S} = \nabla \mathbf{u} + (\nabla \mathbf{u})^{\mathrm{T}}$ is the strain-rate tensor.

The boundary conditions on the rigid plane ($z = 0$) and free surface ($z = 1$) are

$$\mathbf{u} = (u, v, w) = 0, \quad \frac{\partial T}{\partial z} = 0, \quad z = 0, \tag{5}$$

$$\begin{gathered} \tau_{13} + \frac{\partial T}{\partial x} = 0, \quad \tau_{23} + \frac{\partial T}{\partial y} = 0, \quad w = 0, \\ -\frac{\partial T}{\partial z} = Bi \cdot (T - T_\infty) + \tilde{Q}, \quad z = 1. \end{gathered} \tag{6}$$

Here, T_∞ is the temperature of the bound gas far from the surface and $\tilde{Q}$ is the imposed heat flux to the environment.[7]

The solution of basic flow can be determined as follows:

$$\mathbf{u} = (U_0(z), 0, 0), \quad T_0(x, z) = -x + T_b(z). \tag{7}$$

For the linear flow,

$$U_0(z) = z, \quad T_b(z) = Ma \cdot \frac{1}{6}(1 - z^3), \quad \tilde{Q} = \frac{1}{2} Ma, \tag{8}$$

while for the return flow,

$$\begin{gathered} U_0(z) = \frac{3}{4} z^2 - \frac{1}{2} z, \\ T_b(z) = Ma \cdot \left(-\frac{1}{16} z^4 + \frac{1}{12} z^3 - \frac{1}{48}\right), \quad \tilde{Q} = 0. \end{gathered} \tag{9}$$

B. Modal analysis

In the modal analysis, an infinitesimal perturbation in the normal mode form is added to the basic flow,

$$\begin{aligned} (\mathbf{u}, T, P, \boldsymbol{\tau}) = (\mathbf{u}_0, T_0, P_0, \boldsymbol{\tau}_0) + (\widehat{u}, \widehat{v}, \widehat{w}, \widehat{T}, \widehat{P}, \widehat{\boldsymbol{\tau}}) \\ \times \exp\left[i(-\omega t + \alpha x + \beta y)\right]. \end{aligned} \tag{10}$$

Hereafter, the variables without subscript 0 stand for the perturbation. The mode has a complex frequency $\omega = \omega_r + i\omega_i$ and the wave numbers α, β in the x and y directions, respectively. $k = \sqrt{\alpha^2 + \beta^2}$ is the total wave number, and $\phi = \tan^{-1}(\beta/\alpha)$ is the propagation angle.

The linearized governing equations for the perturbation are the same as those in Ref. 48, and the boundary conditions have

$$\widehat{u} = \widehat{v} = \widehat{w} = D\widehat{T} = 0, \quad z = 0, \tag{11}$$

$$\begin{gathered} \widehat{\tau}_{13} + i\alpha \widehat{T} = 0, \quad \widehat{\tau}_{23} + i\beta \widehat{T} = 0, \quad \widehat{w} = 0, \\ D\widehat{T} + Bi \cdot \widehat{T} = 0, \quad z = 1. \end{gathered} \tag{12}$$

TABLE II. Some critical parameters of thermocapillary liquid layers. Here, "a" and "b" stand for the results of Smith and Davis[7] and the present work, respectively. "…" means that the data are not available in the reference.

			Ma		k		ψ		C	
Flow	Pr	Bi	a	b	a	b	a	b	a	b
Linear flow	0.001	1	16.8	17.0	…	0.82	…	90°	…	0.0150
	0.001	0	1.44	1.43	0.096	0.095	90°	90°	0.119	0.119
	0.01	1	14.6	14.5	…	1.2	…	86°	…	0.0101
Return flow	0.001	1	7.2	7.2	…	1.12	…	87°	…	0.0048
	0.01	1	19.3	19.4	…	1.20	…	82°	…	0.0150
	100	0	376	375	2.50	2.48	7.6°	7.5°	0.0624	0.0622

TABLE III. The kinetic energy E_k and temperature energy E_T for the input and output perturbations. Case 1: the linear flow at $Pr = 0.001$, $Ma = 1$, $Bi = 0$, $k = 1$, $\phi = 90°$, and $\omega = -0.015$; case 2: the return flow at $Pr = 100$, $Ma = 300$, $Bi = 0$, $k = 2.5$, $\phi = 0°$, and $\omega = -0.162$.

	Case 1		Case 2	
	Input	Output	Input	Output
E_k	1	3.37×10^5	1	4.10×10^3
E_T	2.74×10^{-4}	2.91×10^3	28.8	7.12×10^5
E_T/E_k	2.74×10^{-4}	8.64×10^{-3}	28.8	1.74×10^2

The perturbation can be obtained in the form of $\mathbf{W}'\hat{\boldsymbol{\psi}} = \omega \mathbf{Z}'\hat{\boldsymbol{\psi}}$, where $\mathbf{W}', \mathbf{Z}'$ are two matrices and $\hat{\boldsymbol{\psi}} = (\hat{u}, \hat{v}, \hat{w}, \hat{T})$. The eigenvalue problem is solved by using the Chebyshev collocation method.[26]

We have computed some critical parameters of thermocapillary liquid layers in Table II. Here, $\psi = 180° - \phi$ and $c = |\omega_r|/k$ is the wave speed. The results agree well with those in Ref. 7.

C. Non-modal analysis

Now, we would like to check if the liquid layer is sensitive to external forcing and restrict our attention to the perturbation with the wave numbers (α, β).

Suppose $\boldsymbol{\psi}(t) = (u, v, w, T)$ is a small perturbation and the flow is driven by a harmonic signal $\boldsymbol{\Theta}$ with the frequency ω in the form

$$\boldsymbol{\Theta} = \exp\left[\mathrm{i}(-\omega t + \alpha x + \beta y)\right]\hat{\boldsymbol{\Theta}}(z), \tag{13}$$

then the evolution equation of $\boldsymbol{\psi}(t)$ is[34]

$$\frac{\partial}{\partial t}\boldsymbol{\psi} = -\mathrm{i}\hat{\mathbf{L}}\boldsymbol{\psi} + \boldsymbol{\Theta}. \tag{14}$$

Here, $\hat{\mathbf{L}} = (\mathbf{Z}')^{-1}\mathbf{W}'$. The maximum response can be defined as the maximum value of amplification,

$$\Re(\alpha, \beta, \omega) = \max_{\boldsymbol{\Theta} \neq 0} \frac{\|\boldsymbol{\psi}\|}{\|\boldsymbol{\Theta}\|} = \|(\omega \mathbf{I} - \hat{\mathbf{L}})^{-1}\|, \tag{15}$$

where $\mathbf{I}$ is the identity matrix. $\|\boldsymbol{\psi}\|$ is the norm of vector $\boldsymbol{\psi}$, which can be defined by the "energy" of disturbance as follows:[49]

$$E = \|\boldsymbol{\psi}\|^2 = \int (|u|^2 + |v|^2 + |w|^2 + \varsigma |T|^2)\mathrm{d}z, \tag{16}$$

where ς is a positive coefficient. The numerical method to compute $\Re$ has been introduced in Refs. 26 and 48.

In the computation, we choose $\varsigma = k^2/100$, which is the same as that in Ref. 48. In Table III, the kinetic energy E_k and temperature energy E_T are displayed for the input and output perturbations, where

$$E_k = \int (|u|^2 + |v|^2 + |w|^2)\mathrm{d}z, \quad E_T = \int \varsigma |T|^2 \mathrm{d}z. \tag{17}$$

All values are normalized by the input kinetic energy. For small Pr, the "energy" of disturbance is mainly a measure of kinetic energy, while for large Pr, it becomes a measure of temperature. However, there are always large amplifications for both the velocity and the temperature. The results are nearly independent of ς when ς is the order of $O(k^2/100)$.

III. NUMERICAL RESULTS

A. Response function

We compute the response function $\Re$ to external excitations for subcritical flows, whose Marangoni number Ma is less than the critical value Ma_c. The maximum response function with a real frequency is defined as[34]

$$\Re^{\max}(\alpha, \beta) = \max_{\omega \in \mathbf{R}} \Re(\alpha, \beta, \omega), \tag{18}$$

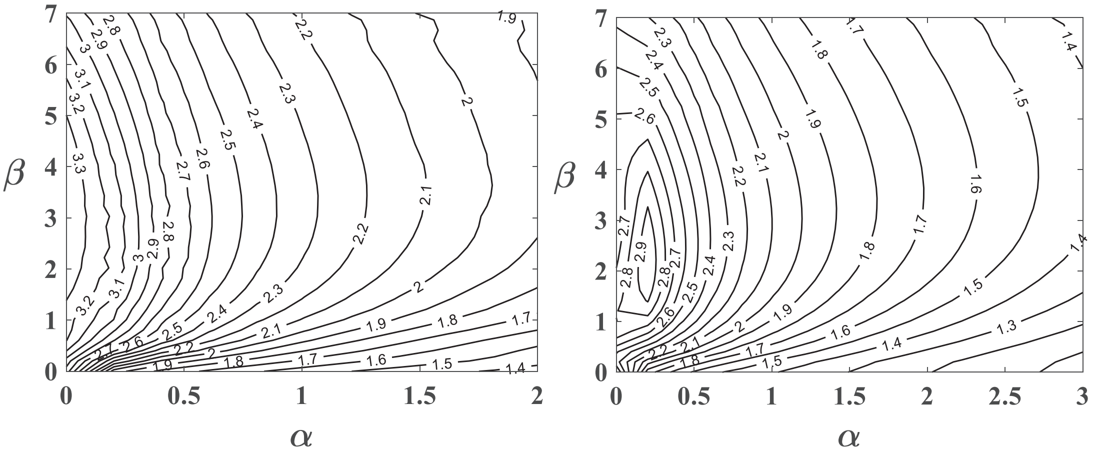

(a) (b)

FIG. 2. Level lines of the logarithm of maximum response $\Re^{\max}$ in the $\alpha - \beta$ plane for the linear flow: (a) $Pr = 0.001$, $Ma = 2$, and $Bi = 1$ and (b) $Pr = 0.01$, $Ma = 10$, and $Bi = 1$.

where **R** denotes the set of real numbers. The optimal response is defined as

$$\Re^{\text{opt}} = \max_{\alpha,\beta} \Re^{\max}(\alpha,\beta), \tag{19}$$

and ω^{opt} is the frequency corresponding to $\Re^{\text{opt}}$. Due to symmetry, we shall confine ourselves to the cases $\alpha \geq 0, \beta \geq 0$.

We examine the maximum response $\Re^{\max}$ with various wave numbers. Figure 2 shows the level lines of $\Re^{\max}$ in the $\alpha - \beta$ plane for subcritical linear flows. The critical Marangoni numbers are Ma_c=17.0 for case (a) and Ma_c=14.5 for case (b). It can be seen that for a wide range of wave numbers, $\Re^{\max}$ could be as large as $O(100)$. When $Pr = 0.001$, the optimal response ($O(\Re^{\text{opt}}) = 1000$) appears in the spanwise direction ($\alpha = 0$) with the wave number $\beta \approx 3$, while the propagation angle corresponding to $\Re^{\text{opt}}$ is close to 90° at Pr =0.01. These properties are similar to those of transient growth (Hu *et al.* 2020). However, an obvious difference from the latter is that there are also large responses ($O(\Re^{\max}) = 100$) in the streamwise direction ($\beta = 0$) in Fig. 2.

The level lines of $\Re^{\max}$ for subcritical return flows are plotted in Fig. 3. The critical Marangoni numbers are $Ma_c = 7.2$ for case(a), $Ma_c = 19.4$ for case(b), and $Ma_c = 375.3$ for case(c). It can be seen that the level lines at small Pr [Figs. 3(a) and 3(b)] are similar to those of linear flow (Fig. 2), which indicates that $\Re^{\max}$ is not very sensitive to the basic flow. However, the structures of the level lines at $Pr = 100$ [see Fig. 3(c)] are quite different from those at small Pr. The optimal response is achieved in the streamwise direction with the wave number $\alpha \approx 2.5$.

We plot the variation of response function $\Re$ with real frequencies for the linear flow in Fig. 4. It can be seen that $\Re$ is relatively large when $\omega \approx 0$ and then decays quickly when $|\omega|$ is large enough [see Figs. 4(a)–4(f)]. In particular, $\Re$ is symmetric with respect to the line

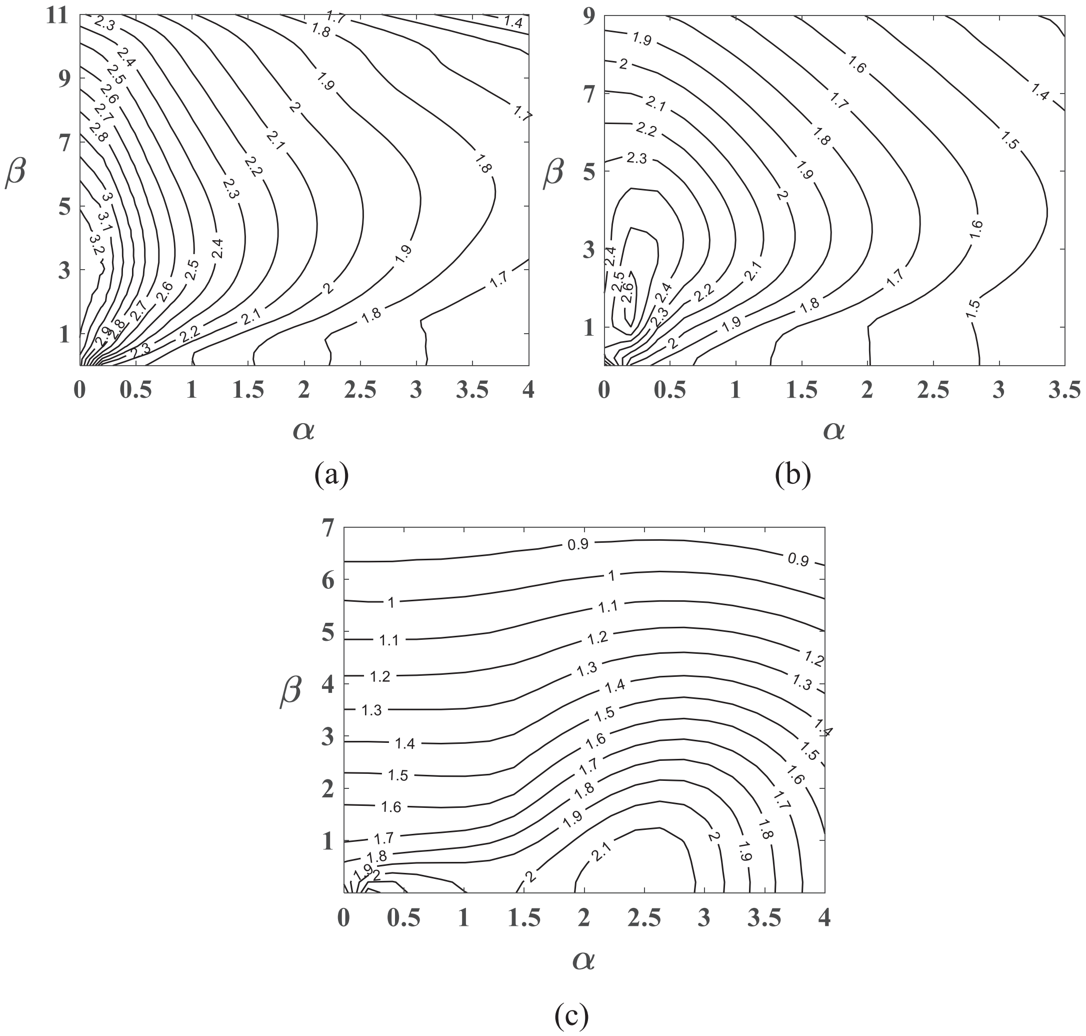

(a)

(b)

(c)

FIG. 3. Level lines of the logarithm of maximum response $\Re^{\max}$ in the $\alpha - \beta$ plane for the return flow: (a) Pr =0.001, $Ma = 3$, and $Bi = 1$; (b) Pr =0.01, $Ma = 12$, and $Bi = 1$; and (c) Pr =100, $Ma = 300$, and $Bi = 0$.

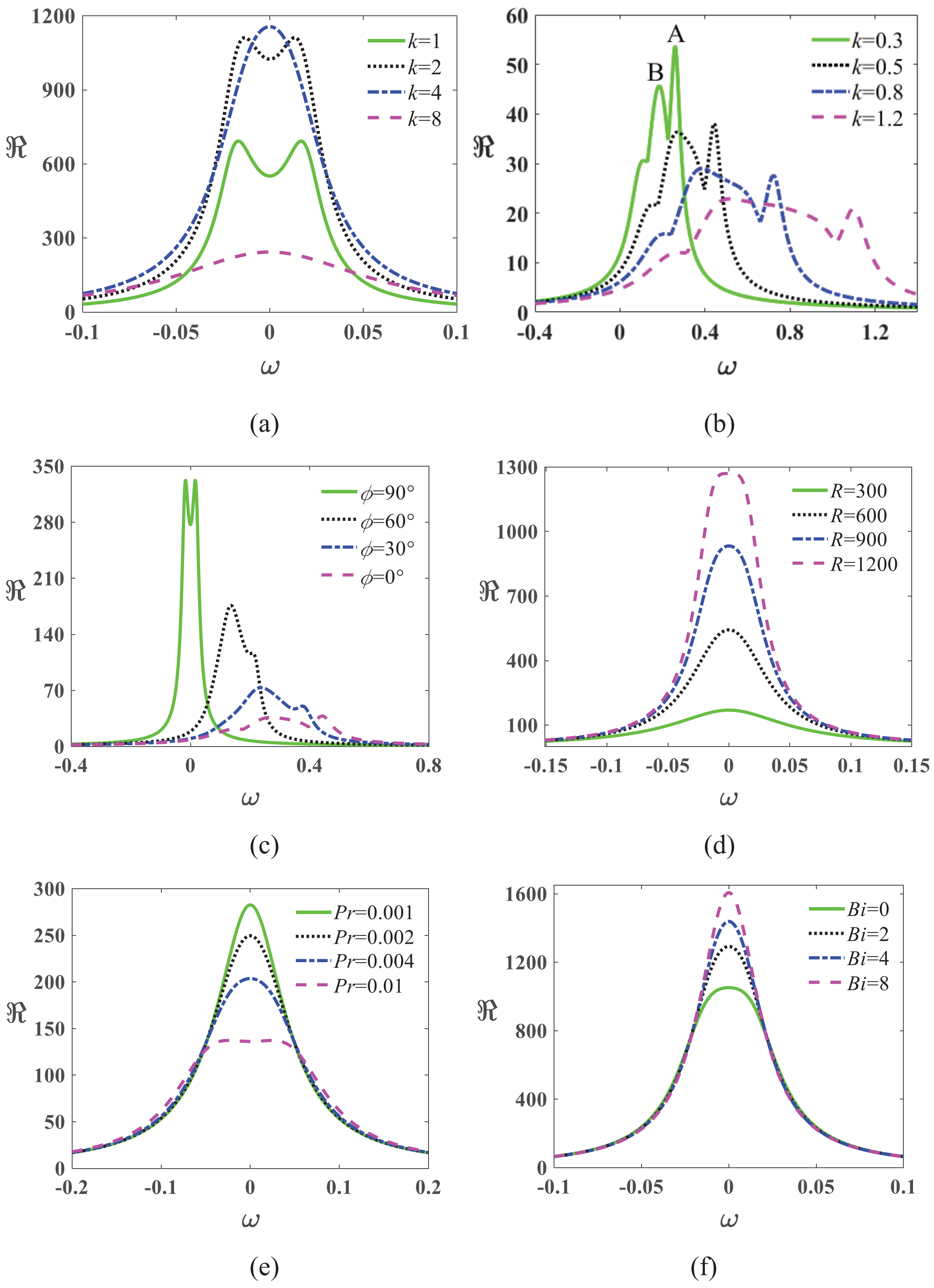

FIG. 4. The response function $\Re$ vs the real frequency of the linear flow: (a) at $Pr = 0.001$, $Ma = 1.2$, and $Bi = 0$, $\phi = 90^\circ$ with various wave numbers k; (b) at $Pr = 0.001$, $Ma = 1$, and $Bi = 0$, $\phi = 0^\circ$ with various wave numbers k; (c) at $Pr = 0.001$, $Ma = 1$, $Bi = 0$, and $k = 0.5$ with various propagation angles ϕ; (d) at $Pr = 0.001$, $Bi = 0$, $k = 3$, and $\phi = 90^\circ$ with various Reynolds numbers R; (e) at $R = 400$, $k = 3$, $Bi = 0$, and $\phi = 90^\circ$ with various Prandtl numbers Pr; and (f) at $Pr = 0.001$, $Ma = 1$, $k = 3$, and $\phi = 90^\circ$ with various Biot numbers Bi.

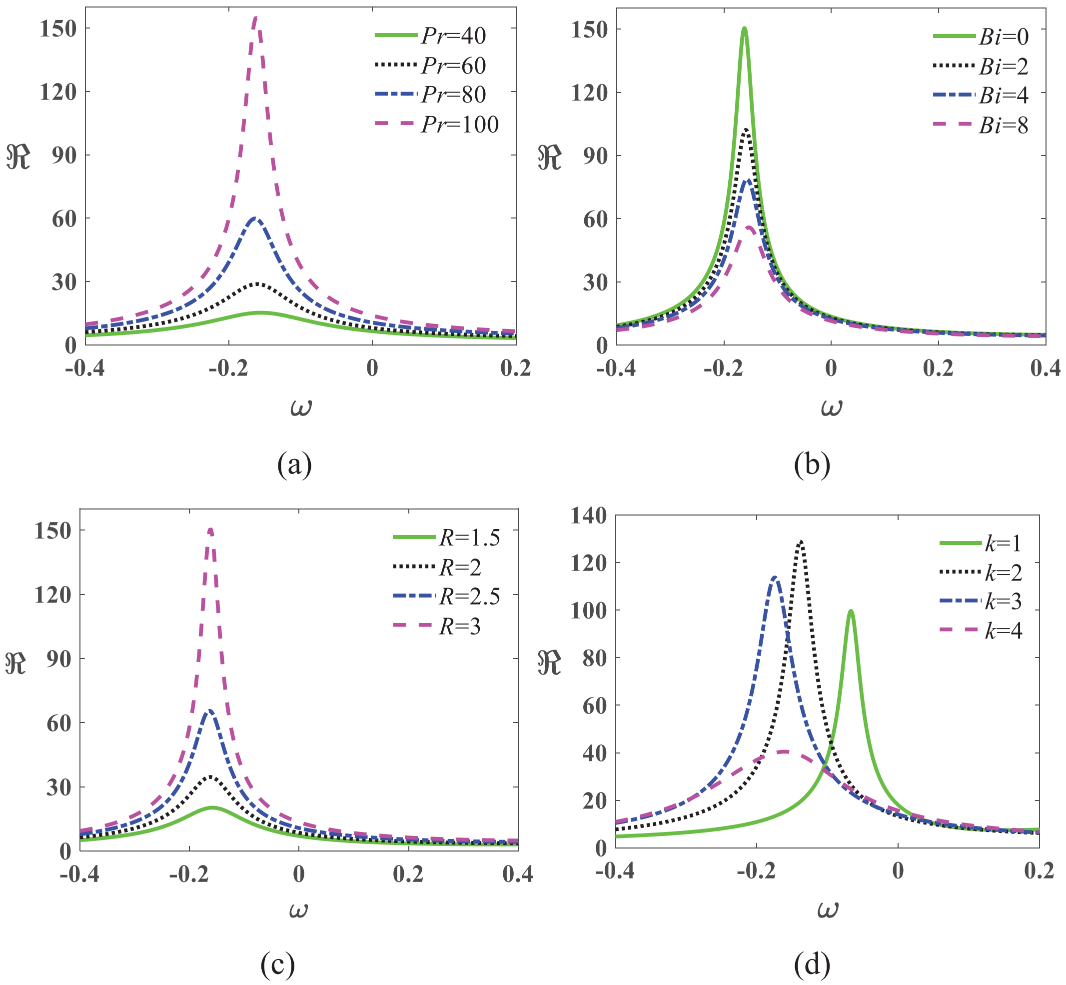

FIG. 5. The response function $\Re$ vs the real frequency of the return flow at $\phi = 0°$ for large *Pr*: (a) at $R = 3$, $k = 2.5$, and $Bi = 0$ with various *Pr* values; (b) at $Ma = 300$, $Pr = 100$, and $k = 2.5$ with various *Bi* values; (c) at $Pr = 100$, $Bi = 0$, and $k = 2.5$ with various *R* values; and (d) at $Ma = 300$, $Pr = 100$, and $Bi = 0$ with various *k* values.

$\omega = 0$ at $\phi = 90°$ [see Figs. 4(a) and 4(d)–(f)]. The maximum response $\Re^{\max}$ is achieved at a moderate wave number when $\phi = 90°$ [see Fig. 4(a)]. By comparing Figs. 4(a), 4(b), and 4(c), we can find that $\Re^{\max}$ is relatively large for streamwise-independent perturbation and decreases significantly with the decrease in ϕ. Figure 4(b) shows that $\Re^{\max}$ decreases with the wave number k when $\phi = 0°$. The peak corresponding to $\Re^{\max}$ is labeled as "A", which has $\omega_A = 0.259$. Another peak is labeled as "B" with $\omega_B = 0.183$. The perturbation flow fields at these two peaks are totally different, which will be discussed in Subsection III C. $\Re$ increases significantly with both R [see Fig. 4(d)] and *Bi* [see Fig. 4(f)] but decreases with *Pr* [see Fig. 4(e)].

For the return flow, the properties of the response function at small *Pr* are similar to those of linear flow. However, we can still find large amplifications in the return flow at large *Pr*. Figure 5 shows the response function of return flow at $\phi = 0°$ for large *Pr*. $\Re^{\max}$ decreases with *Bi* [see Fig. 5(b)] but increases significantly with both *Pr* [see Fig. 5(a)] and R [see Fig. 5(c)]. The variations of $\Re^{\max}$ with *Bi* and *Pr* are in contrast to the cases of linear flow at small *Pr*, which can also be seen from Table IV at different wave numbers. In Fig. 5(d), it can be seen that $\Re^{\max}$ is achieved at a moderate wave number. The frequency corresponding to $\Re^{\max}$ is nearly constant when *Pr*, *Bi,* and R increase. In addition, it is always less than 0, which means that the maximum response wave travels upstream. This agrees with the result of modal

TABLE IV. The variations of $\Re^{\max}$ with *Bi* and *Pr* at different wave numbers.

	$k = 1, \varphi = 30°$			$k = 4, \varphi = 60°$		
Pr	60	80	100	60	80	100
$\Re^{\max}$						
Bi						
0	54.0	69.4	84.7	11.6	18.7	28.9
2	49.6	64.0	78.6	11.0	17.3	26.5
4	47.2	60.9	74.9	10.6	16.4	24.8

analysis,[50] where the hydrothermal wave in the streamwise direction propagates upstream.

B. Pseudospectrum

When the frequency ω is complex, the response function $\Re$ could become larger than the maximum value discussed in Subsection III A. For example, $\|(\omega\mathbf{I}-\hat{\mathbf{L}})^{-1}\| \to \infty$ when ω equals the eigenvalue in modal analysis. In order to study the response function with complex frequency, the "ε-pseudospectrum" was introduced by Trefethen *et al.*[28] as follows:

$$\Lambda_\varepsilon(\hat{\mathbf{L}}) = \{\omega \in C : \|(\omega\mathbf{I}-\hat{\mathbf{L}})^{-1}\| \geq \varepsilon^{-1}\}, \tag{20}$$

where $\varepsilon \geq 0$.

In Fig. 6, the eigenvalues and level lines of pseudospectra for the linear flow at $Pr = 0.001$, $\phi = 90°$, and $Bi = 0$ with different R values are displayed, which correspond to the cases in Figs. 4(a) and 4(d). Most eigenvalues are located in the imaginary axis $\omega_r = 0$. In Fig. 6(a), the least stable mode is stationary ($\omega_r = 0$). When R increases, two traveling waves ($\omega_r \neq 0$) become the least stable modes, and the number of eigenvalues in the range $\omega_i \in [-1, 0]$ increases significantly. However, the variation of R has little influence on the outer contours of pseudospectra. In Fig. 4(a), the peaks of $k = 2$ are reached at $\omega = \pm 0.013$, which are close to the three least stable eigenvalues ($\omega = \pm 0.018 - 0.012\mathrm{i}, -0.022\mathrm{i}$) in Fig. 6(c). By comparing Fig. 4(d) with Fig. 6(a), we can find a similar case at $R = 300$ and $k = 3$. Therefore, the appearance of $\Re^{\max}$ can be attributed to the resonance effect, which occurs when the frequency of input is close to the natural frequency of the system.

In Fig. 7, the eigenvalues and the level lines of pseudospectra for the linear flow at $R = 400$, $k = 3$, $\phi = 90°$, and $Bi = 0$ with different Pr values are displayed, which corresponds to the case in Fig. 4(e). When

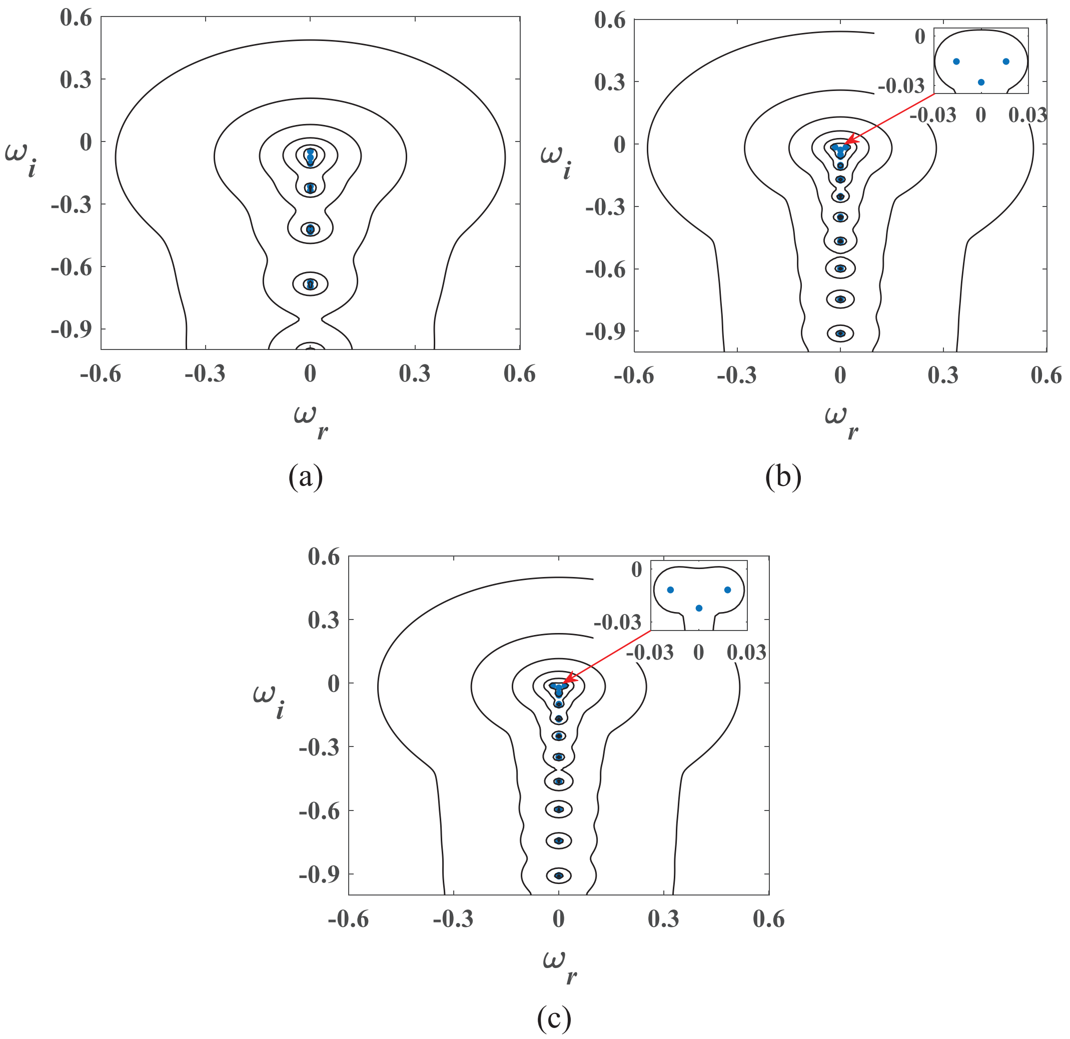

FIG. 6. Pseudospectra for the linear flow at $Pr = 0.001$, $\phi = 90°$, and $Bi = 0$: (a) $R = 300$ and $k = 3$; (b) $R = 1200$ and $k = 3$; and (c) $R = 1200$ and $k = 2$.·: eigenvalues; −: contours from outermost to innermost representing levels from $\varepsilon = 10^{-0.5}$ to 10^{-3} (the spacing of the exponent is 0.5).

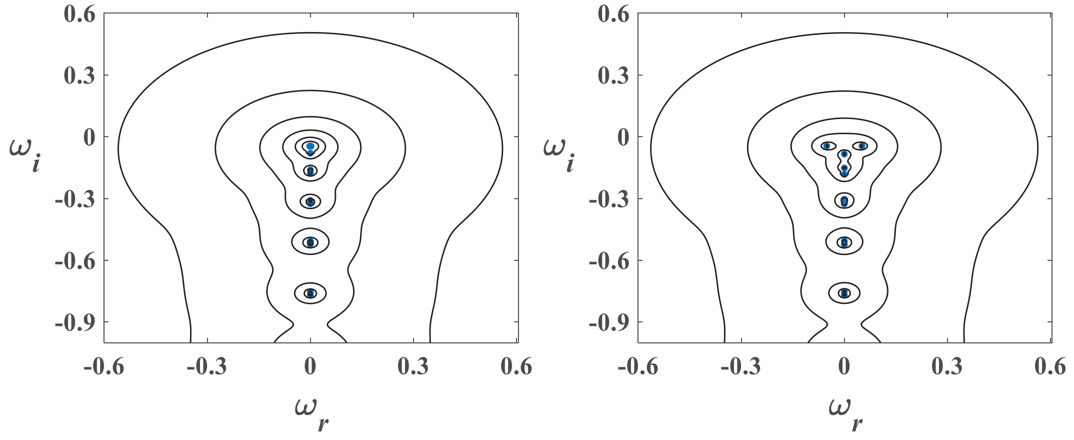

(a) (b)

FIG. 7. Pseudospectra for the linear flow at $R = 400$, $k = 3$, $\phi = 90°$, and $Bi = 0$: (a) $Pr = 0.001$ and (b) $Pr = 0.01$.: eigenvalues; −: contours from outermost to innermost representing levels from $\varepsilon = 10^{-0.5}$ to 10^{-3} (the spacing of the exponent is 0.5).

Pr increases, the least stable mode changes from the stationary mode to the traveling wave. The area of inner contours in the upper half-plane slightly decreases, while there is little change for outer contours.

The eigenvalues and level lines of pseudospectra at $\phi = 0°$ and $Bi = 0$ are displayed in Fig. 8. The cases of Figs. 8(a) and 8(b) correspond to those of Figs. 4(b) and 5(b), respectively. The peaks of the response function are related to the distribution of eigenvalues. In Fig. 4(b), $\omega = 0.259$ at Point A and $\omega = 0.183$ at Point B. In Fig. 8(a), the least stable mode has $\omega_r \approx 0.259$, and there are many eigenvalues in the range $\omega_i \in [-0.2, 0]$ and $\omega_r \approx 0.183$. Therefore, when the frequency of input is close to 0.183 or 0.259, the resonance would appear to cause large amplifications. In Fig. 8(b), the least stable modes listed near the line of $\omega_r = -0.162$ lead to the resonance at this frequency in Fig. 5(b).

$\omega_r < 0$ ($\omega_r > 0$) corresponds to the wave traveling upstream (downstream). Smith[50] has discussed the mechanism of upstream hydrothermal waves at large *Pr*, where the interaction of the interior hot spot with the basic flow is crucial for the propagation direction. For the return flow, the interior hot spot has $U_0 < 0$ and appears upstream of the interfacial hot spot, heating the surface by conduction. Then, the interfacial disturbance propagates upstream. However, we find that the heat convection on the surface ($U_0 i\alpha \widehat{T}$) is the key to the mechanism for the mode with $\omega_r > 0$. As $U_0 > 0$ on the surface, the interfacial hot spot propagates downstream. As the eigenvalue $\omega \approx (1.2 - 0.3\mathrm{i})$ is far from the real axis $\omega_i = 0$ and other eigenvalues, this mode has little effect on $\mathfrak{R}^{\max}$.

C. Input and output fields

In this subsection, we pay attention to the perturbation field corresponding to the maximum response.

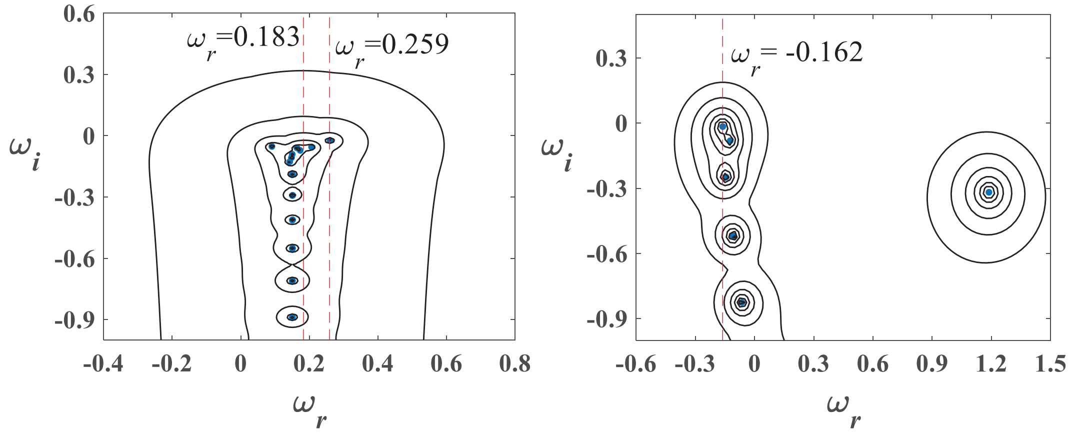

(a) (b)

FIG. 8. Pseudospectra at $\phi = 0°$ and $Bi = 0$: (a) the linear flow, $Pr = 0.001$, $Ma = 1$, and $k = 0.3$; (b) the return flow, $Pr = 100$, $Ma = 300$, and $k = 2.5$.: eigenvalues; −: contours from outermost to innermost representing levels from $\varepsilon = 10^{-0.5}$ to 10^{-3} (the spacing of the exponent is 0.5).

The perturbation fields corresponding to the maximum response for the linear flow are displayed in Fig. 9. The parameters are the same as those of case 1 in Table III. It can be seen that both the input and output fields are characterized by counter-rotating vortices and streamwise streaks (narrow regions where the streamwise velocity is larger or smaller than the average), which are similar to the flow fields of the optimal transient growth.[48] The magnitudes of output temperature and velocity are far larger than those of input.

The perturbation fields displayed in Figs. 10 and 11 correspond to Point B and Point A in Fig. 2(b), respectively. It can be seen that $v = 0$ in Fig. 10, while $u = w = 0$, $T = 0$ in Fig. 11. Therefore, these two perturbation fields are similar to the Orr–Sommerfeld (OS) modes and Squire (SQ) modes in plane shear flows,[26] respectively. In Fig. 10, the amplification of external excitation is mainly caused by the increase in $|u|$ and the vortices are spanwise. In Fig. 11, there is only a perturbation for the spanwise velocity, whose amplitude appears on the free surface.

The perturbation fields corresponding to the maximum response for the return flow at $Pr = 100$ are displayed in Fig. 12. The parameters are the same as those of case 2 in Table III. We can find that both the velocity and the temperature are significantly amplified. The input velocity and temperature mainly distribute in the region near the surface, which differs from the cases at small Pr.

IV. DISCUSSION

In this section, we discuss the amplification mechanism of thermocapillary liquid layers and make comparisons with the cases in other flows.

The energy mechanism can be seen from the equation for the output kinetic energy,[48]

$$\begin{aligned}\frac{\partial E_k}{\partial t} &= -\frac{1}{2R}\int(\boldsymbol{\tau}:\mathbf{S})\mathrm{d}^3r + \frac{1}{R}\int\mathbf{u}\cdot\boldsymbol{\tau}\cdot\mathbf{n}\mathrm{d}^2r\\ &\quad - \int\mathbf{u}\cdot((\mathbf{u}\cdot\nabla)\mathbf{u}_0)\mathrm{d}^3r + \int\mathbf{u}\cdot\mathbf{F}^{in}\mathrm{d}^3r\\ &= -N + M + I + \Psi,\end{aligned} \tag{21}$$

where $\mathbf{F}^{in}$ is the input force, N is the viscous dissipation, M is the work done by Marangoni forces on the surface, I is the energy from the basic flow, and Ψ is the input energy. In Table V, we list the terms in (21) normalized by the kinetic energy $\int|\mathbf{u}|^2d^3r = 1$.

For small Pr, M is negligible, so

$$\frac{\partial E_k}{\partial t} \approx -N - \int uw\cdot DU_0\mathrm{d}^3r + \Psi. \tag{22}$$

The insensitivity of $\Re^{\max}$ to the basic flow in Figs. 2 and 3 can be explained by the energy mechanism. It can be seen from (22) that $|uw\cdot DU_0|$ is crucial for the amplification of kinetic energy. However, this term is relatively large in the region $z \in [0.3, 0.8]$, as $|uw|$ becomes very small near the boundaries. Figure 1 shows that the velocity distributions of two flows are similar at $z \in [0.3, 0.8]$. Thus, the difference in basic flow has little impact on the level lines of $\Re^{\max}$.

The perturbation at $\phi = 90°$ displayed in Fig. 9 shows that for the input signal, the magnitude of streamwise velocity is far smaller than those of normal and spanwise velocities, whereas the opposite is

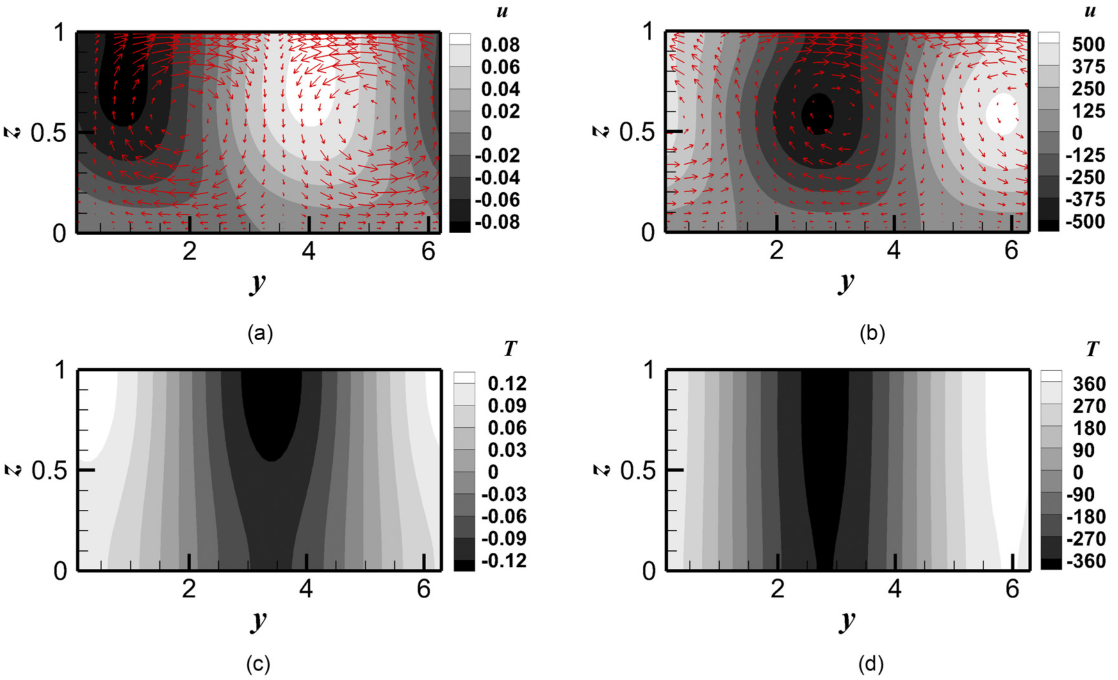

(a) (b) (c) (d)

FIG. 9. The perturbation fields corresponding to the maximum response for the linear flow at $Pr = 0.001$, $Ma = 1$, $Bi = 0$, $k = 1$, and $\phi = 90°$: (a) the input velocity field; (b) the output velocity field; (c) the input temperature field; and (d) the output temperature field. The maximum growth is $\Re^{\max} = 583$ at $\omega = -0.015$. The amplitudes of input are $|u| = 0.0873$, $|v| = 1.1797$, $|w| = 0.2978$, and $|T| = 0.1402$, while the amplitudes of output are $|u| = 520.4437$, $|v| = 53.0067$, $|w| = 10.4785$, and $|T| = 392.0727$.

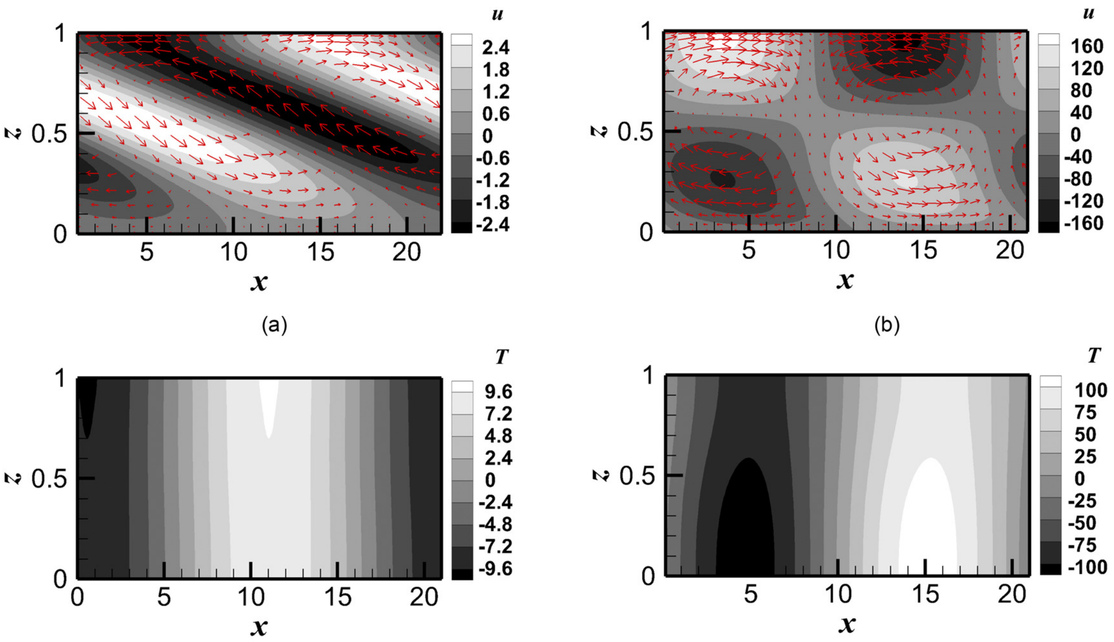

(a) (b) (c) (d)

FIG. 10. The perturbation fields corresponding to the response for the linear flow at $Pr = 0.001$, $Ma = 1$, $Bi = 0$, $k = 0.3$, and $\phi = 0°$: (a) the input velocity field; (b) the output velocity field; (c) the input temperature field; and (d) the output temperature field. The response is $\Re = 45.7$ at $\omega = 0.183$. The amplitudes of input are $|u| = 2.8730$, $|v| = 0$, $|w| = 0.2093$, and $|T| = 9.7319$, while the amplitudes of output are $|u| = 168.4013$, $|v| = 0$, $|w| = 14.3955$, and $|T| = 114.1777$.

true for the output field. The perturbation equation in the x-direction can be simplified as

$$\frac{\partial u}{\partial t} + w \cdot DU_0 - \frac{1}{R}\nabla^2 u = f_x^{in}, \tag{23}$$

where u and w are the output velocities, $\frac{1}{R}\nabla^2 u$ is the viscous force, and f_x^{in} is the input force in the x-direction. The terms of (23) for the perturbation in Fig. 9 are listed in Table VI, which suggest that the amplification of the streamwise velocity u is mainly caused by the vertical velocity w and the velocity gradient of basic flow DU_0, while the input force is nearly zero. This mechanism has been known as the "lift-up" effect,[34,51] where the streamwise streaks are amplified from streamwise vortices.

For the perturbation at $\phi = 0°$ in Fig. 10, the output perturbation extracts energy from the basic flow and the input force (see case 2 of Table V). In addition, the spanwise velocity $v = 0$. Thus, the amplification is caused by a combination of the external disturbance and the two-dimensional Reynolds stress mechanism (also called the Orr mechanism).[34] For the perturbation in Fig. 11, $M = I = 0$, and so the amplification is only due to Ψ. In total, we have seen three kinds of amplification mechanisms, which are more complicated than those in channel flows.

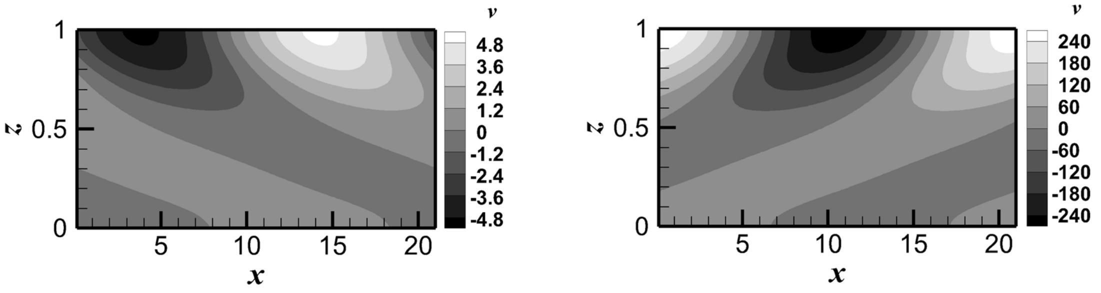

(a) (b)

FIG. 11. The perturbation fields corresponding to the maximum response for the linear flow at $Pr = 0.001$, $Ma = 1$, $Bi = 0$, $k = 0.3$, and $\phi = 0°$: (a) the input field and (b) the output field. The maximum response is $\Re^{max} = 53.7$ at $\omega = 0.259$. The amplitudes of input are $|u| = 0$, $|v| = 5.0585$, $|w| = 0$, and $|T| = 0$, while the amplitudes of output are $|u| = 0$, $|v| = 271.8655$, $|w| = 0$, and $|T| = 0$.

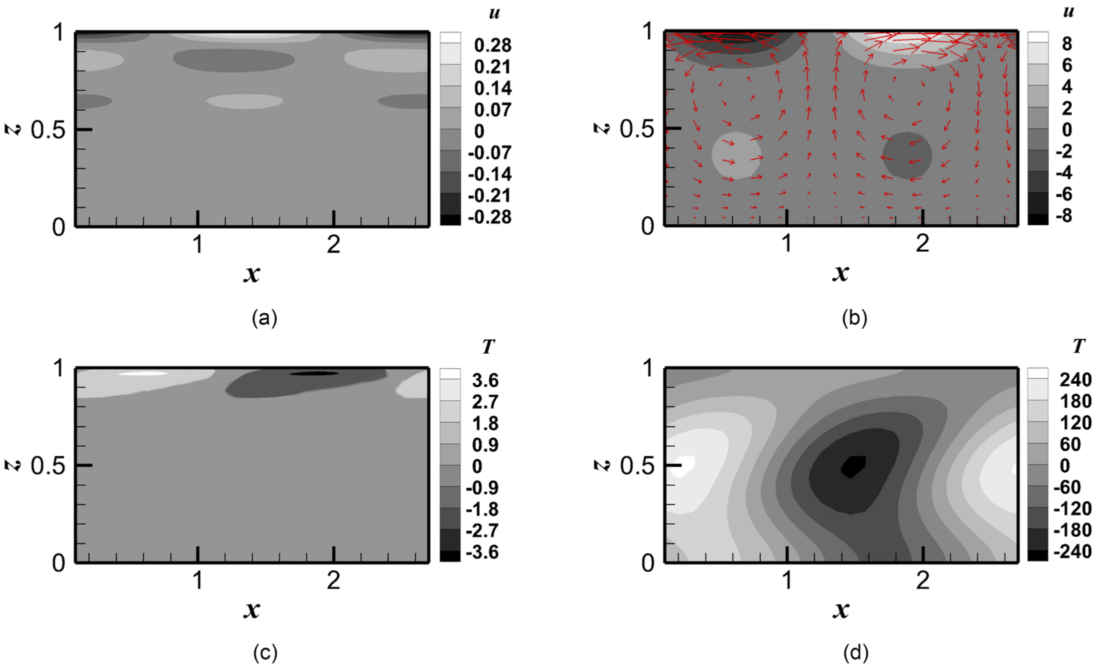

FIG. 12. The perturbation fields corresponding to the maximum response for the return flow at $Pr = 100$, $Ma = 300$, $Bi = 0$, $k = 2.5$, and $\phi = 0°$: (a) the input velocity field; (b) the output velocity field; (c) the input temperature field; and (d) the output temperature field. The maximum response is $\Re^{\max} = 154.9$ at $\omega = -0.162$. The amplitudes of input are $|u| = 0.2989$, $|v| = 0$, $|w| = 0.0211$, and $|T| = 3.7687$, while the amplitudes of output are $|u| = 8.9889$, $|v| = 0$, $|w| = 2.6798$, and $|T| = 243.9798$.

It seems from the energy analysis that the effect of Marangoni force is only driving the basic flow for small *Pr*. However, we should be aware of the particularity of the Marangoni effect on thermocapillary liquid layers. Many free surface flows are susceptible to surface deformations, while the surface of the thermocapillary liquid layer is assumed to be non-deformable because of the surface tension. So there is a restriction on its surface: $w = 0$. On the other hand, the thermocapillary liquid layer has less constraint on the upper boundary than channel flows, as the former could have horizontal velocity perturbations on its surface. This boundary condition is crucial for the perturbations in Figs. 9–12. We can see that the horizontal velocity near the surface is amplified significantly, which is very important for $\Re$. Specifically, in Figs. 10–12, the amplitude of output velocity appears on the surface, which does not exist in channel flows. Therefore, it is the particularity of the boundary condition in the thermocapillary liquid layer that induces these kinds of perturbations with large amplifications.

TABLE V. The terms in (21) for the most amplified disturbances. Cases 1–4 correspond to Figs. 9–12, respectively.

	Case 1	Case 2	Case 3	Case 4
Pr	0.001	0.001	0.001	100
N	0.004 957	0.022 860	0.015 860	14.13 579
M	0.000 067	0.000 179	0	14.12 762
I	0.004 636	0.008 825	0	0.003 297
Ψ	0.000 254	0.013 857	0.015 860	0.004 873

In thermocapillary liquid layers, the temperature field on the surface has a negative effect on the hydrodynamic instability.[48] The increase in *Bi* reduces the temperature perturbation on the surface, and so $\Re^{\max}$ increases with the increase in *Bi* for small *Pr* in Fig. 4(f). The amplification for small *Pr* decreases obviously with *Pr* in Fig. 4(e). This can be seen from the following definitions: $R = \rho b \gamma d^2/\mu^2$, $Pr = \mu/(\rho\chi)$. When $\mu \to 0.1\mu$ and $\rho \to 0.01\rho$, we have $R \to R$, $Pr \to 10Pr$, and $\nu = \mu/\rho \to 10\nu$. This indicates that when *R* remains constant, the increase in *Pr* corresponds to the increase in kinematic viscosity, which can inhibit the hydrodynamic instability and stabilize the flow.

For large *Pr*, the Reynolds numbers are only the order of 1 in Fig. 5, which suggests that the amplification mechanism is not hydrodynamic. It can be seen from Table V that the work done by Marangoni is far larger than the energy from the basic flow and the external disturbance at large *Pr*. In addition, the importance of *M* increases with *Pr*. Thus, the temperature field is crucial and the amplification is caused by the thermocapillary effect. The increase in *Bi*

TABLE VI. The terms of (23) for the perturbation in Fig. 9 at different positions.

(y, z)	$\frac{\partial u}{\partial t}$	$w \cdot DU_0$	$-\frac{1}{R}\nabla^2 u$	f_x^{in}
$(2.5, 0.3)$	-1.1416	2.0048	-0.8958	-0.0327
$(2.5, 0.7)$	-2.0137	2.0164	-0.0897	-0.0870
$(5.5, 0.3)$	1.5112	-2.1983	0.7188	0.0317
$(5.5, 0.7)$	2.6294	-3.1753	0.6330	0.0871

reduces the temperature perturbation on the surface and leads to the decrease in $\Re^{\max}$ in Fig. 5(b). Smith[50] found that the thermocapillary instability in the liquid layer at large *Pr* is caused by the vertical heat convection. When *Pr* increases, the convection becomes more important in the heat transfer. Therefore, the amplification increases with *Pr* in Fig. 5(a).

In Fig. 12(a), the input velocity and temperature are mainly distributed in the region near the surface, which makes the input energy rather small. Meanwhile, the thermocapillary effect caused by input temperature on the surface induces the counter-rotating vortices and large temperature perturbations in the layer [see Fig. 12(b)]. Therefore, the response function could achieve $O(100)$. However, if the input field becomes the initial perturbation in the evolution of transient growth, the velocity gradient is very large near the surface, which leads to high dissipation. Thus, there is no obvious transient growth at large *Pr*.[48]

The results in this paper demonstrate that the amplification of external forcing is more obvious than that of initial disturbance. As the transient growth function $G(t) = \sup_{\boldsymbol{\psi}(0)\neq 0} \|\boldsymbol{\psi}(t)\|^2/\|\boldsymbol{\psi}(0)\|^2$,[48] while the response function $\Re(\omega) = \max_{\boldsymbol{\Theta}\neq 0}\|\boldsymbol{\psi}\|/\|\boldsymbol{\Theta}\|$, we should compare $|\Re(\omega)|^2$ with $G(t)$. For the linear flow at $Pr = 0.001$, $Bi = 0$, $k = 3$, $\phi = 90°$, and $G^{\max} = \max_{t\geq 0} G(t) = 165.8$, while $|\Re^{\max}|^2 = 1.61 \times 10^6$. Furthermore, $\Re^{\max}$ could reach $O(100)$ for a wide range of wave numbers, while large transient growths $G^{\max} \approx O(100)$ mainly appear at $k = 3$ and $\varphi \approx 90°$. In addition, we have shown several kinds of amplification mechanisms for external excitations at small and large *Pr*. On the contrary, the transient growth caused by the hydrodynamic mechanism only occurs at small *Pr*.[48] It seems that the thermocapillary liquid layer is more sensitive to the background noise than to the initial condition.

When the interface deformation is considered, there is less constraint on the surface, the flow can be destabilized. In addition, a new kind of mode, namely, the surface wave, could be excited in the layer.[52] As the surface-wave instability is most prominent at small *Pr* and hydrodynamic in nature,[5] we could expect that this destabilization effect is more obvious at small *Pr*.

The heating of a liquid layer may produce evaporation. For a weak evaporation, the basic flow is not obviously affected by the mass flux on the surface. The increase in evaporation only leads to the increase in heat exchange, which corresponds to a larger *Bi*. Therefore, the amplification would be increased by the evaporation at small *Pr*, while the opposite happens at large *Pr*. However, in the case of the rapid evaporation, the experiment[53] shows that the vapor recoil can directly trigger the flow instability.

The liquid layer is similar to many thermocapillary-driven films, such as the thermocapillary migration of droplet, which is placed on a unidirectional heated solid surface and flattened by gravity,[3,19] and nanofluid films with flat interfaces.[4,54,55] In addition, previous works suggest that thermocapillary instabilities found in horizontal layers also appear in cylindrical geometries, such as the liquid bridge of crystal growth[9] and the liquid jet of inkjet printing.[2] Therefore, the disturbance amplification presented may also exist in the above cases. The understanding of the amplification mechanism is useful for the stability control in these applications.

V. CONCLUSION

We examine the responses to external excitations for thermocapillary liquid layers by non-modal stability theory. In order to study the maximum amplification of input signals, the response function $\Re$ is defined by the perturbation velocity and temperature. The results show that there can be rather large amplifications in subcritical flows at both small and large Prandtl numbers (*Pr*). The flow is more sensitive to the external noise than to the initial disturbance.

For small *Pr*, the maximum response $\Re^{\max}$ increases significantly with both the Reynolds number *R* and the Biot number *Bi*, but decreases with *Pr*. The optimal response occurs when the propagation angle of perturbation $\phi \approx 90°$ and the wave number is moderate ($k \approx 3 \sim 4$). Large responses appear for a wide range of wave numbers, including the case of streamwise waves ($\beta = 0$). The properties of $\Re^{\max}$ for the return flow and the linear flow are similar. The amplification is due to a combination of the lift-up mechanism, Orr mechanism, and external forcing.

For large *Pr*, $\Re$ is very small for the linear flow. However, $\Re^{\max}$ could be $O(100)$ in subcritical return flows. In contrast to the case at small *Pr*, $\Re^{\max}$ increases with *Pr* but decreases with *Bi*. The optimal response is achieved when the perturbation is a streamwise wave. The variations of the frequency corresponding to $\Re^{\max}$ with *Pr*, *Bi*, and *R* are negligible. The amplification is attributed to the thermocapillary effect.

Pseudospectra suggest that the resonance effect occurs when the frequency of external excitation is close to the eigenvalue of the least stable modes. The variations of *R* and *Pr* have little influence on the outer contours of pseudospectra. When *Pr* increases, the least stable mode changes from the stationary mode to the traveling wave, and the area of inner contours in the upper half-plane slightly decreases for small *Pr*.

For both small and large *Pr*, there are large amplifications for both the velocity and the temperature. When $\phi = 90°$, the input and output flow fields are characterized by counter-rotating vortices and streamwise streaks. When $\phi = 0°$, there are two kinds of fields similar to the Orr-Sommerfeld (OS) modes and Squire (SQ) modes in plane shear flows.

ACKNOWLEDGMENTS

This work was supported by the National Natural Science Foundation of China (Nos. 11872032, U1738119, and 11772344), the Zhejiang Provincial Natural Science Foundation (No. LY21A020006), the K. C. Wong Magna Fund, and the Special research funding from the Marine Biotechnology and Marine Engineering Discipline Group in Ningbo University (No. 422004582).

DATA AVAILABILITY

The data that support the findings of this study are available within this article.

REFERENCES

[1] T. Dufar, *Crystal Growth Processes Based on Capillarity: Czochralski, Floating Zone, Shaping and Crucible Techniques* (John Wiley & Sons, 2010).

[2] J. J. Xu and S. H. Davis, "Instability of capillary jets with thermocapillarity," J. Fluid Mech. **161**, 1–25 (1985).

[3] W. Q. Dai, M. M. Khonsari, C. Shen, and X. Wang, "Thermocapillary migration of liquid droplets induced by a unidirectional thermal gradient," Langmuir **32**(30), 7485–7492 (2016).

[4] S. Maity, "Thermocapillary flow of thin Cu-water nanoliquid film during spin coating process," Int. Nano Lett **7**(1), 1–15 (2017).

[5] S. H. Davis, "Thermocapillary instabilities," Annu. Rev. Fluid Mech. **19**(1), 403–435 (1987).

[6] M. F. Schatz and G. P. Neitzel, "Experiments on thermocapillary instabilities," Annu. Rev. Fluid Mech. **33**(1), 93–127 (2001).

[7] M. K. Smith and S. H. Davis, "Instabilities of dynamic thermocapillary liquid layers. Part 1.Convective instabilities," J. Fluid Mech. **132**, 119–144 (1983).

[8] T. Watanabe, Y. Kowata, and I. Ueno, "Flow transition and hydrothermal wave instability of thermocapillary-driven flow in a free rectangular liquid film," Int. J. Heat Mass Transfer **116**, 635–641 (2018).

[9] M. Wanschura, V. Shevtsova, H. Kuhlmann, and H. Rath, "Convective instability mechanisms in thermocapillary liquid bridges," Phys. Fluids **7**, 912–925 (1995).

[10] C. Y. Yan, K. X. Hu, and Q. S. Chen, "Thermocapillary instabilities of liquid layers on an inclined plane," Phys. Fluids **30**(8), 082101 (2018).

[11] A. C. Or and R. E. Kelly, "Thermocapillary and oscillatory-shear instabilities in a layer of liquid with a deformable surface," J. Fluid Mech. **360**, 21–39 (1998).

[12] B. L. Smorodin, A. B. Mikishev, A. A. Nepomnyashchy, and B. I. Myznikova, "Thermocapillary instability of a liquid layer under heat flux modulation," Phys. Fluids **21**(6), 062102 (2009).

[13] S. Yang, R. Liang, and J. He, "Oscillating characteristic of free surface from stability to instability of thermocapillary convection for high Prandtl number fluids," Int. J. Heat Fluid **61**, 298–308 (2016).

[14] T. Yamamoto, Y. Takagi, Y. Okano, and S. Dost, "Numerical investigation of oscillatory thermocapillary flows under zero gravity in a circular liquid film with concave free surfaces," Phys. Fluids **28**(3), 032106 (2016).

[15] K. X. Hu, M. He, and Q. S. Chen, "Instability of thermocapillary liquid layers for Oldroyd-B fluid," Phys. Fluids **28**(3), 033105 (2016).

[16] K. X. Hu, M. He, Q. S. Chen, and R. Liu, "Linear stability of thermocapillary liquid layers of a shear-thinning fluid," Phys. Fluids **29**, 073101 (2017).

[17] K. X. Hu, M. He, Q. S. Chen, and R. Liu, "Effect of gravity on the stability of viscoelastic thermocapillary liquid layers," Int. J. Heat Mass Transfer **123**, 776–786 (2018).

[18] K. X. Hu, M. He, Q. S. Chen, and R. Liu, "On the stability of thermocapillary convection of a Bingham fluid in an infinite liquid layer," Int. J. Heat Mass Transfer **122**, 993–1002 (2018).

[19] K. X. Hu, C. Y. Yan, and Q. S. Chen, "Instability of thermocapillary-buoyancy convection in droplet migration," Phys. Fluids **31**, 122101 (2019).

[20] L. A. Davalos-Orozco, "Sideband thermocapillary instability of a thin film flowing down the outside of a thick walled cylinder with finite thermal conductivity," Int. J. Non-Linear Mech. **109**, 15–23 (2019).

[21] L. Zhang, Y. R. Li, C. M. Wu, and Q. S. Liu, "Flow bifurcation routes to chaos of thermocapillary convection for low Prandtl number fluid in shallow annular pool with surface heat dissipation," Int. J. Therm. Sci. **125**, 23–33 (2018).

[22] Q. Kang, J. Wang, L. Duan, Y. Su, J. He, D. Wu, and W. Hu, "The volume ratio effect on flow patterns and transition processes of thermocapillary convection," J. Fluid Mech. **868**, 560–583 (2019).

[23] R. J. Riley and G. P. Neitzel, "Instability of thermocapillary–buoyancy convection in shallow layers. Part 1. Characterization of steady and oscillatory instabilities," J. Fluid Mech. **359**, 143–164 (1998).

[24] Y. R. Li, N. Imaishi, T. Azami, and T. Hibiya, "Three-dimensional oscillatory flow in a thin annular pool of silicon melt," J. Cryst. Growth **260**, 28–42 (2004).

[25] P. G. Drazin, *Introduction to Hydrodynamic Stability* (Cambridge, 2002).

[26] P. J. Schmid and D. S. Henningson, *Stability and Transition in Shear Flows* (Springer, 2001).

[27] P. J. Schmid, "Nonmodal stability theory," Annu. Rev. Fluid Mech. **39**, 129–162 (2007).

[28] L. N. Trefethen, A. E. Trefethen, S. C. Reddy, and T. A. Driscoll, "Hydrodynamic stability without eigenvalues," Science **261**(5121), 578–584 (1993).

[29] S. J. Davies and C. M. White, "An experimental study of the flow of water in pipes of rectangular section," Proc. R. Soc., A **119**(781), 92–107 (1928).

[30] W. Pfenninger, "Boundary layer suction experiments with laminar flow at high reynolds numbers in the inlet length of a tube by various suction methods," in Boundary Layer Flow Control (1961), pp. 961–980.

[31] M. Nishioka, S. Iida, and Y. Ichikawa, "An experimental investigation of the stability of plane Poiseuille flow," J. Fluid Mech. **72**, 731–756 (1975).

[32] H. Schlichting, *Boundary-Layer Theory* (McGraw-Hill, 1979).

[33] C. Nouar, N. Kabouya, J. Dusek, and M. Mamou, "Modal and non-modal linear stability of the plane Bingham–Poiseuille flow," J. Fluid Mech. **57**, 211–239 (2007).

[34] R. Liu and Q. S. Liu, "Non-modal instability in plane Couette flow of a power-law fluid," J. Fluid Mech. **676**, 145–171 (2011).

[35] R. Liu and Q. S. Liu, "Non-modal stability in sliding Couette flow," J. Fluid Mech. **710**, 505–544 (2012).

[36] V. C. Patel and M. R. Head, "Some observations on skin friction and velocity profiles in fully developed pipe and channel flows," J. Fluid Mech. **38**, 181–201 (1969).

[37] N. Tillmark and P. H. Alfredsson, "Experiments on transition in plane Couette flow," J. Fluid Mech. **235**, 89–102 (1992).

[38] I. J. Wygnanski, M. Sokolov, and D. D. Friedman, "On transition in a pipe. Part 2. The equilibrium puff," J. Fluid Mech. **69**(02), 283–304 (1975).

[39] H. C. Kuhlmann and U. Schoisswohl, "Flow instabilities in thermocapillary-buoyant liquid pools," J. Fluid Mech. **644**, 509–535 (2010).

[40] J. H. Han, Z. W. Sun, L. R. Dai, J. C. Xie, and W. R. Hu, "Experiment on the thermocapillary convection of a mercury liquid bridge in a floating half zone," J. Cryst. Growth **169**, 129–135 (1996).

[41] N. Garnier and A. Chiffaudel, "Two dimensional hydrothermal waves in an extended cylindrical vessel," Eur. Phys. J. B. **19**, 87–95 (2001).

[42] B. C. Sim, A. Zebib, and D. Schwabe, "Oscillatory thermocapillary convection in open cylindrical annuli. Part 2. Simulations," J. Fluid Mech. **49**, 1259–1274 (2003).

[43] R. Shari, K. Kyoko, J. M. Carroll, R. O. M. Grigoriev, and F. Schatz, "Transient Amplification and Contact Line Instability," in *Division of Fluid Dynamics 56th Annual Meeting*, November 23–25, East Rutherford, New Jersey (American Physical Society, 2003).

[44] R. O. Grigoriev, "Contact line instability and pattern selection in thermally driven liquid films," Phys. Fluids **15**(6), 1363–1374 (2003).

[45] J. Rieser, see http://people.maths.ox.ac.uk/porterm/research/jen_final.pdf for "Transient Amplification and Contact Line Instability (2005)"

[46] J. M. Davis, D. E. Kataoka, and S. M. Troian, "Transient dynamics and structure of optimal excitations in thermocapillary spreading: Precursor film model," Phys. Fluids **18**(9), 579–106 (2006).

[47] F. Doumenc, T. Boeck, B. Guerrier, and M. Rossi, "Transient Rayleigh–Bénard–Marangoni convection due to evaporation: A linear non-normal stability analysis," J. Fluid Mech. **648**, 521–539 (2010).

[48] K. X. Hu, S. Zheng, and Q. S. Chen, "Transient growth in thermocapillary liquid layers," Phys. Rev. Fluids **5**, 014001 (2020).

[49] A. Sameen and R. Govindarajan, "The effect of wall heating on instability of channel flow," J. Fluid Mech. **577**, 417–442 (2007).

[50] M. K. Smith, "Instability mechanisms in dynamic thermocapillary liquid layers," Phys. Fluids **29**(10), 3182–3186 (1986).

[51] M. T. Landahl, "A note on an algebraic instability of inviscid parallel shear flows," J. Fluid Mech. **98**, 243–251 (1980).

[52] M. K. Smith and S. H. Davis, "Instabilities of dynamic thermocapillary liquid layers. Part 2. Surface-wave instabilities," J. Fluid Mech. **132**, 145–162 (1983).

[53] J. J. Li, L. Zhang, L. Zhang, Y. R. Li, and X. J. Quan, "Experimental study on the effect of surface evaporation on the thermocapillary-buoyancy convection in a shallow annular pool," Int. J. Heat Mass Transfer **140**, 828–836 (2019).

[54] S. Maity, Y. Ghatani, and B. S. Dandapat, "Thermocapillary flow of a thin nanoliquid film over an unsteady stretching sheet," J. Heat Transfer **138**(4), 1–8 (2016).

[55] A. A. Abdullah, N. M. Alraiqib, and K. A. Lindsay, "Modelling the stability of Marangoni convection in a layer of nanofluid," J. Therm. Sci. **151**, 106228 (2020).